

Alternating twisted multilayer graphene: generic partition rules, double flat bands, and orbital magnetoelectric effect

Bo Xie,¹ Shihao Zhang,¹ and Jianpeng Liu^{1,2}

¹*School of Physical Science and Technology, ShanghaiTech University, Shanghai 200031, China*

²*ShanghaiTech laboratory for topological physics, ShanghaiTech University, Shanghai 200031, China*

(Dated: January 17, 2022)

Twisted graphene systems have drawn significant attention due to the discoveries of various correlated and topological phases. In particular, recently the alternating twisted trilayer graphene is discovered to exhibit unconventional superconductivity, which motivates us to study the electronic structures and possible interesting correlation effects of this class of alternating twisted graphene systems. In this work we consider generic alternating twisted multilayer graphene (ATMG) systems with M - L - N stacking configurations, in which the M (L) graphene layers and the L (N) layers are twisted by an angle θ ($-\theta$). Based on analysis from a simplified $\mathbf{k}\cdot\mathbf{p}$ model approach, we analytically derive generic partition rules for the low-energy electronic structures, which exhibit various intriguing band dispersions including one pair of flat bands, two pairs of flat bands, as well as flat bands co-existing with Dirac cones, quadratic bands, or more generally $E(\mathbf{k}) \sim k^J$ dispersions (J is positive integer) for each spin and valley. Such unusual non-interacting electronic structures may have unconventional correlation effects. Especially for a mirror symmetric ATMG system with two pairs of flat bands (per spin per valley), we find that Coulomb interactions may drive the system into a state breaking both time-reversal and mirror symmetries, which can exhibit a novel type of orbital magnetoelectric effect due to the intertwining of electric polarization and orbital magnetization orders in the symmetry-breaking state.

The recent discoveries of some intriguing phenomena, such as superconductivity¹⁻⁸, quantum anomalous Hall effect⁹⁻¹⁵, and correlated insulator states^{4-7,9,16-21} in magic-angle twisted bilayer graphene (TBG) has aroused great interest. In magic-angle TBG²², the interlayer moiré potential generates pseudo magnetic fields, which are coupled with the Dirac fermions from the two layers, leading to topological non-trivial flat bands with eight-fold degeneracy with valley, spin and sublattice degrees of freedom²³⁻²⁸. Such degeneracy can be split by strong Coulomb interactions, leading to symmetry-breaking states reminiscent of quantum Hall ferromagnetism. The interplay between non-trivial topology and strong Coulomb interaction give rise to fruitful physics in magic angle TBG²⁹⁻⁵⁷.

The intriguing flat-bands physics is not unique for magic-angle TBG. It has been theoretically proposed and experimentally observed that topologically nontrivial flat bands with strong correlation effects can also exist in twisted multilayer systems such as twisted bilayer-monolayer graphene and twisted double bilayer graphene^{16,58-67}. Moreover, recently unconventional superconductivity has been observed in alternating twist trilayer graphene⁶⁸⁻⁷¹, which is a new type of twisted graphene system with topologically nontrivial flat bands co-existing with dispersive Dirac cone around the charge neutrality point (CNP)^{72,73}. This motivates us study the electronic structures and correlation effects of alternating twisted multilayer graphene systems. One would expect that the extra twist may fundamentally change the low-energy electronic structures, and the extra layers may introduce additional degrees of freedom that may give rise to versatile interaction effects⁷⁴⁻⁷⁶.

In this work, we theoretically study alternating twisted

multilayer graphene (ATMG) : a class of twisted graphene consisting of three sequences of stacking graphene with alternating twist angle, denoted as $M - L - N$. We describe the low energy physics in the non-interaction regime with a continuum model. We classify them by low energy band dispersion for each spin and valley into three types, including one pair of flat bands, one pair of flat bands co-exist with Dirac cone (quadratic bands) and $E(\mathbf{k}) \sim k^J$ (J is positive integer), and two pairs of flat bands co-exist with $E(\mathbf{k}) \sim k^J$ (J is positive integer). Based on an analytic analysis from a simplified $\mathbf{k}\cdot\mathbf{p}$ model approach, which exclude the redundancy parts of the continuum model, we find that the low energy band structure can be described by a generic partition rule. According to the partition rule, there must be double flat bands for ATMG with mirror m_z symmetry and more than one layers in the middle sequence. Finally, we consider Coulomb interaction effects and screening effects from remote bands in $A - ABA - A$ (with two pairs of flat bands). We study the ground states at different integer filling factors under zero external field. It turns out that the mirror symmetry can be broken spontaneously by Coulomb interaction. Besides, a calculation under finite vertical electric field indicates that the electric field can enhance the orbital magnetization linearly.

I. CONTINUUM MODEL FOR ATMG

In this work we consider a class of alternating twisted multilayer graphene (ATMG), which consist of three sets of graphene multilayers with the number of layers denoted by M , L , N respectively. The stacking sequence within each set of multilayers can be Bernal (ABA),

rhombohedral (ABC), or a mixture of the two. These multilayers are stacked from bottom to up in the M - L - N sequence, where the N (L) layers and the L (M) layers are twisted by an angle θ ($-\theta$) as schematically shown in Fig. 1(a). Such a system forms a moiré pattern in real space with the moiré superlattice constant $L_s = a/(2\sin\theta/2)$, where $a = 2.46 \text{ \AA}$ is the graphene lattice constant. The corresponding moiré Brillouin zone is shown in Fig. 1(b). Similar to twisted bilayer graphene (TBG), the low energy states of the ATMG system are contributed by those from the atomic K and K' valleys, which are approximately decoupled from each other at the non-interacting level for small twist angles. Thus, it is generally assumed that the system preserves valley charge conservation at small twist angles²². Therefore, we generalize the Bistritzer-MacDonald continuum model²² to describe the low-energy states of the ATMG system for each valley and each spin, assuming the states from the K and K' valleys are completely decoupled. The continuum model for valley μ ($\mu = \mp$ for K and K' valleys) is expressed as

$$H_{ATMG}^\mu = \begin{pmatrix} H_N^\mu & \mathbb{U}_\mu^\dagger e^{-i\mu\Delta\mathbf{K}\cdot\mathbf{r}} & 0 \\ \mathbb{U}_\mu e^{i\mu\Delta\mathbf{K}\cdot\mathbf{r}} & H_L^\mu & \mathbb{U}_\mu e^{i\mu\Delta\mathbf{K}\cdot\mathbf{r}} \\ 0 & \mathbb{U}_\mu^\dagger e^{-i\mu\Delta\mathbf{K}\cdot\mathbf{r}} & H_M^\mu \end{pmatrix} \quad (1)$$

where H_N^μ , H_L^μ and H_M^μ denote the $\mathbf{k}\cdot\mathbf{p}$ Hamiltonians of the untwisted graphene multilayers, which consist of the Dirac fermions of each monolayer graphene and the interlayer hopping terms. $\mathbb{U}_\mu e^{i\mu\Delta\mathbf{K}\cdot\mathbf{r}}$ stands for the moiré potential term for valley μ , which arises from the mutual twist between two sets of adjacent multilayers. $\Delta\mathbf{K} = (0, 4\pi/(3L_s))$ is a vector characterizing the shift of Dirac points due to the twist. The details of the

continuum Hamiltonian Eq. (1) are presented in Supplementary Information.

II. GENERIC PARTITION RULES

One can obtain various types of low-energy band structures from the Hamiltonian given by Eq. (1). A careful study reveals that the ATMG systems can be roughly divided into three types based on their low-energy band dispersion: for type (i) there is only one pair of flat bands for each valley and spin, which is similar to TBG; for type (ii) there is one pair of flat bands co-existing with some low-energy bands characterized by the dispersion $E(\mathbf{k}) \sim k^J$ (J is positive integer); and for type (iii) there are two pairs of flat bands. In Fig. 1(c)-(d) we show the band structures of two typical ATMG systems with $A-A-A$ and $A-ABA-A$ stacking, where the solid and dashed lines denote energy bands from the K and K' valleys respectively in chiral limit, i.e the intrasublattice coupling between twisted layers are zero. For the $A-A-A$ system, there is one pair of flat bands co-existing with a Dirac cone (per valley per spin), which can be categorized as type (ii) ATMG; while there are two pairs of flat bands for each valley and spin for the $A-ABA-A$ system, which is the simplest example of type (iii) ATMG. In what follows we will explain the origin of such intriguing low-energy dispersion and derive partition rules for generic ATMG systems.

To better illustrate the origin of these intriguing low-energy dispersion, we first consider the chiral limit in which all the intrasublattice couplings are turned off. Within the chiral limit, we first analyze the low-energy states of the untwisted multilayers, then discuss the effects of the moiré potentials at the twisted interfaces. It has been proposed that an untwisted multilayer graphene with arbitrary stacking sequence and with the total number of layers N can be decomposed into S_N chiral segments, within each of which the stacking chirality is unchanged. Then the low-energy states contributed by the i th chiral segment with the number of layers J_i consists of a chiral doublet described by the following effective Hamiltonian

$$H_{J_i}^\mu(\mathbf{k}) \propto k^{J_i} [\cos(J_i\phi_{\mathbf{k}})\sigma_x \pm \sin(J_i\phi_{\mathbf{k}})\sigma_y] \quad (2)$$

where $\tan\phi_{\mathbf{k}} = k_y/k_x$, and $\sigma_{x,y}$ denote Pauli matrices in the sublattice space. Then the low-energy Hamiltonian of the untwisted N layers from valley μ can be written as a direct sum of those of the N_D chiral segments:

$$H_N^\mu \approx H_{J_1}^\mu \oplus H_{J_2}^\mu \dots \oplus H_{J_{S_N}}^\mu. \quad (3)$$

Each segment contributes to a chiral doublet with the dispersion $E \sim k^{J_i}$ around \mathbf{K}^μ point. Then we consider the chirally decomposed N layers are stacked with the other M layers and are twisted by angle θ . The moiré potential at the interface would couple the topmost chiral segment of the N with the bottom-most segment of the

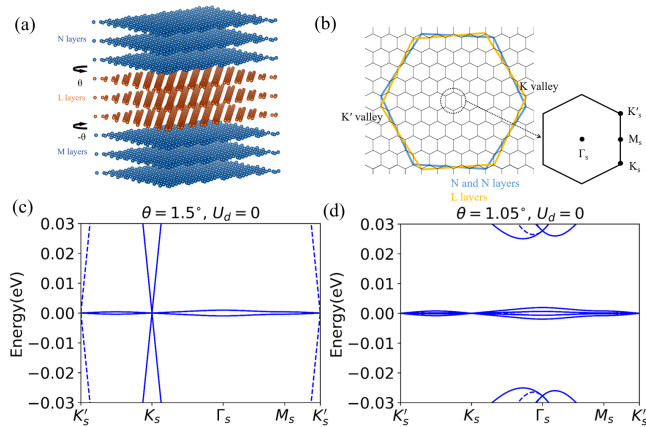


FIG. 1: (a) Lattice structure of alternating twist multilayer graphene. (b) Brillouin zones of M , L and N layers and Moiré Brillouin zone with high symmetry points. Band structure of (c) $A-A-A$ and (d) $A-ABA-A$ at K valley (solid line) and K' valley (dashed line) in the chiral limit, considering nearest neighbor interlayer hopping.

M layers, giving rise to a pair of flat bands for each spin and each valley. These flat bands would co-exist with the dispersive chiral doublets contributed by the remaining chiral segments (if any) of the two sets of multilayers⁷⁷. The ATMG system introduces additional complexity due to the additional multilayers (L layers) and the additional twist. It turns out that the situations with the number of middle layers $L = 1$ and $L > 1$ need to be treated separately.

To evaluate the difference between ATMG systems with $L = 1$ and $L > 1$, we first consider alternating twisted trilayer graphene (TTG), i.e. $M = L = N = 1$. We will show that for TTG, in which three alternating twisted layers are coupled together, can be decoupled into a TBG-like Hamiltonian and a free Dirac-fermion Hamiltonian. For the sake of convenience, we first apply a gauge transformation to the basis functions of the ATMG system:

$$\tilde{\psi}_{ls,\mathbf{k}}^\mu(\mathbf{r}) = \psi_{ls,\mathbf{k}}^\mu(\mathbf{r}) e^{i\mathbf{K}_l^\mu \cdot \mathbf{r}} \quad (4)$$

where \mathbf{K}_l^μ denotes the Dirac point of valley μ and layer l , and s is the sublattice index. Such a gauge transformation would remove the phase factor $e^{i\pm\mu\Delta\mathbf{K}\cdot\mathbf{r}}$ in the moiré potential term, and would move the Dirac points of the different twisted layers to the same origin. Then we apply a unitary transformation to the alternating TTG Hamiltonian, $\tilde{H}_{TTG}^\mu = W^\dagger H_{TTG}^\mu W$. The Hamiltonian after the unitary transformation \tilde{H}_{TTG}^μ is expressed as

$$\tilde{H}_{TTG}^\mu = \begin{pmatrix} h^\mu(\mathbf{k}) & 0 & \sqrt{2}U_\mu \\ 0 & h^\mu(\mathbf{k}) & 0 \\ \sqrt{2}U_\mu^\dagger & 0 & h^\mu(\mathbf{k}) \end{pmatrix}, \quad (5)$$

where $h^\mu(\mathbf{k}) = -\hbar v_F \mathbf{k} \cdot \boldsymbol{\sigma}_\mu$, with the Pauli matrices $\boldsymbol{\sigma}_\mu = (\mu\sigma_x, \sigma_y)$ defined in the sublattice space, and the unitary transformation matrix W is expressed as

$$W = \begin{pmatrix} 0 & -\frac{1}{\sqrt{2}} & \frac{1}{\sqrt{2}} \\ 1 & 0 & 0 \\ 0 & \frac{1}{\sqrt{2}} & \frac{1}{\sqrt{2}} \end{pmatrix}. \quad (6)$$

From Eq. (5) it is immediately seen that the total Hamiltonian of alternating twisted trilayer graphene consists of a TBG-like part with the moiré potential rescaled by $\sqrt{2}$ and a free Dirac fermion part. The TBG part and Dirac fermion part are completely decoupled from each other, which contribute to one pair of flat bands co-existing with a Dirac cone as shown in Fig. 1(c). Moreover, since the magic angle is determined by the ratio between the intersublattice component of the moiré potential and the Fermi velocity, the re-scaled moiré potential in Eq. (5) implies that the magic angle for the TTG system is rescaled by the same factor, i.e., the new magic angle should be $\sqrt{2} \times 1.05^\circ \approx 1.5^\circ$.

For $L = 1$ but $M, N > 1$, one can apply the chiral decomposition rule as discussed in Eqs. (2)-(3) to the M layers and N layers. The topmost chiral segment from

the M layer and the bottom-most segment from the N layers are coupled with the $L=1$ middle layer through the moiré potentials, contributing to one pair of flat bands co-existing with either a Dirac cone or a pair of quadratic bands. The remaining chiral segments (if any) in the N layers and M layers would contribute to additional $E(\mathbf{k}) \sim k^J$ dispersive bands. On the other hand, when $L > 1$, one need to apply the chiral decomposition rule to the L multilayers as well, and carefully study how the chiral doublets contributed by the M , L , and N layers are coupled to each other through the moiré potentials at the two twisted interfaces.

After a comprehensive theoretical analysis based on a simplified $\mathbf{k} \cdot \mathbf{p}$ model approach (to be explained in the following section), we have derived a set of generic partition rules describing the low-energy band structures of ATMG systems in the chiral limit. First, the M , L , and N multilayers are divided into S_M , S_L , and S_N chiral segments (see Eqs. (2)-(3)), and the number of layers of the i th segment, say, in N multilayer is denoted as $J_{N,i}$ ($i = 1, \dots, S_N$). We also need to keep the chiral segments that are closest to the twisted interfaces to be as long as possible, i.e., we need to make a choice of chiral decomposition to make J_{M,S_M} , $J_{L,1}$, J_{L,S_L} and $J_{N,1}$ as large as possible. Based on the above choice of chiral segments, we reach the following partition rules for the low-energy dispersion in the chiral limit:

(a) For $L = 1$: the J_{M,S_M} , $J_{L,1}$ and $J_{N,1}$ chiral segments are coupled through the moiré potential generated by the alternating twisted structure. When the stacking chirality of J_{M,S_M} and $J_{N,1}$ are the same, there are one pair of flat bands and one Dirac cone co-existing near \mathbf{K}_μ point (per spin per valley); while if J_{M,S_M} and $J_{N,1}$ have opposite stacking chiralities, there are one pair of flat bands and one pair of quadratic bands co-existing near \mathbf{K}_μ point. The remaining chiral segments in the M (N) multilayers would contribute to additional chiral doublets with the dispersion $E(\mathbf{k}) \sim k^{J_{M,i}}$ ($E(\mathbf{k}) \sim k^{J_{N,i}}$) near \mathbf{K}_μ (\mathbf{K}'_μ) point.

(b) For $L > 1$: if the L multilayer can be divided into more than one chiral segments ($S_L > 1$), there are two pairs of flat bands (double flat bands) around CNP; while if the L multilayer is in the chiral (or rhombohedral) stacking sequence ($S_L = 1$), there is only one pair of flat bands. When $S_L > 1$, the remaining chiral segment $\{J_{L,i}, 2 \leq i \leq S_L - 1\}$ that are not coupled with the M and N multilayers would contribute to dispersive bands $E(\mathbf{k}) \sim k^{J_{L,i}}$ around CNP. Similarly, the remaining chiral segments $\{J_{M,i}, 1 \leq i \leq S_M - 1\}$ ($\{J_{N,i}, 2 \leq i \leq S_N\}$) from the M (N) multilayer that are not coupled with the middle L multilayer would contribute to the low-energy dispersive bands with $E(\mathbf{k}) \sim k^{J_{M,i}}$ ($E(\mathbf{k}) \sim k^{J_{N,i}}$).

In Table I, we illustrate some ATMG systems as typical cases and apply the partition rules described above to these systems to characterize their low energy band structures, where the notation (m, n) means that there are m pairs of bands with dispersion $E(\mathbf{k}) \sim \mathbf{k}^n$ around

TABLE I: Typical cases for generic partition rules. The band structures are measured with full continuum model considering nearest neighbor for untwisted bands. We label m bands with dispersion $E(\mathbf{k}) \sim \mathbf{k}^n$ at $\mathbf{K}_\mu(\mathbf{K}'_\mu)$ as (m,n).

partitioning	number of falt bands	bands at \mathbf{K}	bands at \mathbf{K}'
A-A-A	2	(1,1)	0
A-A-AB+AC	2	(1,1),(1,2)	0
AB-A-BA	2	(1,1)	0
AB-A-AB	2	(1,2)	0
A-AB+A-A	4	0	0
A-ABC-A	2	/	/
A-AB+ABC-A	4	0	0
A+BA-AB+A+BA-AB+A	4	(1,1)	(2,1)

K_s or K'_s points. For example, for *A-A-ABAC* system, it can be divided into two parts including the alternating twisted layers *A-A-AB* and untwisted layers *AC*. The twisted layers would contribute one pair of flat bands co-existing with a Dirac cone around K_μ point, while the untwisted layers give rise to a pair of quadratic bands($E(\mathbf{k}) \sim \mathbf{k}^2$) centered at K_μ point.

III. SIMPLIFIED $\mathbf{k} \cdot \mathbf{p}$ MODEL

The partition rules presented above can be derived using a simplified $\mathbf{k} \cdot \mathbf{p}$ model approach. In this approach, we write a $\mathbf{k} \cdot \mathbf{p}$ model within the moiré Brillouin zone by expanding the flat bands and the Dirac cones around the moiré K_s or K'_s points including the coupling terms between them. In the chiral limit both the flat bands and the Dirac cone can be solved exactly²³, then we can analytically construct a greatly simplified $\mathbf{k} \cdot \mathbf{p}$ model in the basis of the zero modes (flat-band wavefunctions) and the Dirac fermions, and solve it exactly. From the analytic solutions of the simplified $\mathbf{k} \cdot \mathbf{p}$ model, we derive the partition rules for generic ATMG systems presented above. Such an approach can capture the essential low-energy physics, while neglecting the irrelevant high-energy bands obtained from a direct numerical diagonalization of the original continuum Hamiltonian.

To construct such a simplified $\mathbf{k} \cdot \mathbf{p}$ model for a generic ATMG system (in the chiral limit), we should first find proper unitary transformations to the original continuum Hamiltonian to decompose it into a form consisting of a TBG-like continuum Hamiltonian and free Dirac fermions, e.g., as illustrated in Eq. (5). To be specific, for any ATMG system with $L=1$, we can apply the unitary transformation given by Eq. (6) to the three alternating twisted layers, and keep other layers unchanged. The corresponding layer-mixed basis functions are:

$$\begin{aligned}
\bar{\psi}_{\alpha s, \mathbf{k}}^\mu(\mathbf{r}) &= \tilde{\psi}_{Ls, \mathbf{k}}^\mu(\mathbf{r}) \\
\bar{\psi}_{\beta s, \mathbf{k}}^\mu(\mathbf{r}) &= \frac{-1}{\sqrt{2}} \tilde{\psi}_{Ms, \mathbf{k}}^\mu(\mathbf{r}) + \frac{1}{\sqrt{2}} \tilde{\psi}_{Ns, \mathbf{k}}^\mu(\mathbf{r}) \\
\bar{\psi}_{\gamma s, \mathbf{k}}^\mu(\mathbf{r}) &= \frac{1}{\sqrt{2}} \tilde{\psi}_{Ms, \mathbf{k}}^\mu(\mathbf{r}) + \frac{1}{\sqrt{2}} \tilde{\psi}_{Ns, \mathbf{k}}^\mu(\mathbf{r})
\end{aligned} \quad (7)$$

where α, β, γ are the three mix-layer indices marking the basis functions after the unitary transformation, $\psi_{ls, \mathbf{k}}^\mu(\mathbf{r})$ with $l = M, L, N$ denote the basis wave functions (after the gauge transformation of Eq. (4)) of the three alternating twisted layers in the M, L , and N sequence respectively, and $s = A, B$ is the sublattice index. After such a transformation, the continuum Hamiltonian consists of a TBG-like part and a free Dirac fermion (as shown in Eq. (5)) contributed by the three alternating twisted layers, with the terms from the other layers being unchanged. One can solve for the zero-mode solutions for the TBG-like part at the renormalized magic angle $\sqrt{2} \times 1.05^\circ$, and expand all the Dirac cones around the Dirac points within the moiré Brillouin zone, then eventually obtain a $\mathbf{k} \cdot \mathbf{p}$ model in a greatly simplified form. For $L > 1$, above transformation is unnecessary, since there are two pairs of twisted layers giving rise to two TBG-like terms. For each of the TBG-like terms, we can obtain the zero-mode solution of magic-angle TBG in the chiral limit. The analytical wave functions for the zero modes in magic-angle TBG in the chiral limit are expressed as²³:

$$\begin{aligned}
\Psi_{lA, \mathbf{k}}(\mathbf{r}) &= f_{\mathbf{k}}(z) \bar{\psi}_{lA, \mathbf{K}}(\mathbf{r}), \\
\Psi_{lB, \mathbf{k}}(\mathbf{r}) &= f_{\mathbf{k}}^*(-z) \bar{\psi}_{lB, \mathbf{K}}(\mathbf{r})
\end{aligned} \quad (8)$$

where $l = \alpha, \gamma$ refers to the two mix-layer indices as defined in Eq. (7), $\Psi_{ls, \mathbf{K}}(\mathbf{r})$ refers to the s ($s = A, B$) sublattice component of the zero-mode solution at the Dirac point \mathbf{K} ²³. $f_{\mathbf{k}}(z) = \vartheta_{a_1, b_1}(z) / \vartheta_{a_2, b_2}(z)$, where $\vartheta_{a, b}(z)$ is the theta function defined in the previous work²³. For the untwisted layers, we take the $\mathbf{k} \cdot \mathbf{p}$ Hamiltonians of the Dirac fermions and expand them around the Dirac points within the moiré Brillouin zone. The coupling between the zero modes from the twisted layers and the Dirac fermions from the untwisted layers can be evaluated by re-expressing the original interlayer hopping matrix in the basis of the zero-mode wavefunctions and the free Dirac-fermion states.

We take the *AB-A-AB* and *AB-A-BA* stacked ATMG systems as two typical examples to illustrate how the partition rule (a) works. Following the procedures described above, we obtain the simplified $\mathbf{k} \cdot \mathbf{p}$ Hamiltonian for *AB-A-AB* (*AB-A-BA*) stacked ATMG system:

$$H_{\mathbf{k}, \mathbf{p}}^\mu = \begin{pmatrix} h^\mu(\mathbf{k}) & 0 & -h_+ & \tilde{h}_+ & 0 \\ 0 & 0 & 0 & 0 & 0 \\ -h_- & 0 & h^\mu(\mathbf{k}) & 0 & h_{+(-)} \\ \tilde{h}_- & 0 & 0 & 0 & \tilde{h}_{+(-)} \\ 0 & 0 & h_{-(+)} & \tilde{h}_{-(+)} & h^\mu(\mathbf{k}) \end{pmatrix}, \quad (9)$$

where

$$h_+ = \begin{pmatrix} 0 & 0 \\ t_\perp & 0 \end{pmatrix}, \tilde{h}_+ = \begin{pmatrix} 0 & 0 \\ \tilde{t}_\perp & 0 \end{pmatrix} \quad (10)$$

$h^\mu(\mathbf{k}) = -\hbar v_F \mathbf{k} \cdot \boldsymbol{\sigma}^\mu$, and $h_- = h_-^\dagger$ for different stacking chirality. The “+(-)” sign in $\tilde{h}_{+(-)}$ in Eq. (9) applies to

the $AB-A-AB$ ($AB-A-BA$) stacking. t_{\perp} is the interlayer intersublattice hopping parameter. In the chiral limit we only consider nearest neighbor interlayer hopping term, and \tilde{t}_{\perp} is the renormalized hopping parameter. We refer the readers to Supplementary Information(Appendix II) for more details about the simplified $\mathbf{k} \cdot \mathbf{p}$ model.

We present the band structures of the above two ATMG systems in Fig. (2). In particular, in Fig. 2(a)-(b) we show the band structures for $AB-A-AB$ and $AB-A-BA$ systems obtained from direct numerical diagonalizations of the full continuum Hamiltonian in chiral limit, while in Fig. 2(c)-(d) the band structures are calculated by the 10×10 simplified $\mathbf{k} \cdot \mathbf{p}$ model expanded around either K_s or K'_s point as given by Eq. (9). For the $AB-A-AB$ system there are two flat bands co-existing with a Dirac cone (Fig. 2(a) and (c)), while for the $AB-A-BA$ system there are two flat bands and one pair of quadratic band touching around K_s (K'_s) for K (K') valley. We see that the 10×10 simplified $\mathbf{k} \cdot \mathbf{p}$ model can fully capture the essential low-energy physics, which fulfills the partition rules introduced above.

IV. ORIGIN OF DOUBLE FLAT BANDS

Some of the ATMG systems may have two pairs of flat bands (double flat bands) for each valley and spin. According to the partition rules, the double flat bands can only occur when $S_L > 1$. To illustrate the origin of the double flat bands, we first study two ATMG systems for $L = 3$ with $A-ABA-A$ (with double flat bands) and $A-ABC-A$ (with one pair of flat bands) stacking based on

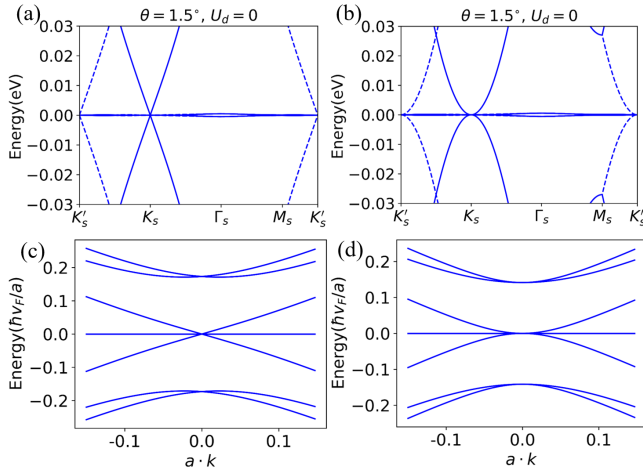


FIG. 2: The band structures of $AB-A-AB$ for K valley (solid line) and K' valley (dashed line) obtained from (a) continuum model and (c) simplified $\mathbf{k} \cdot \mathbf{p}$; $AB-A-BA$ for K valley obtained from (b) continuum model and (d) simplified $\mathbf{k} \cdot \mathbf{p}$ model. The continuum models are constructed including nearest neighbor interlayer hopping and intersublattice moiré potential.

the simplified $\mathbf{k} \cdot \mathbf{p}$ model. To be specific, the simplified $\mathbf{k} \cdot \mathbf{p}$ Hamiltonian of the $A-ABA-A$ system can be written as a direct sum of a 6×6 matrix and two zero modes

$$H_{A-ABA-A}^{\mathbf{k} \cdot \mathbf{p}} = \begin{pmatrix} 0 & \tilde{h}_+ & 0 \\ \tilde{h}_- & h(\mathbf{k}) & \tilde{h}_- \\ 0 & \tilde{h}_+ & 0 \end{pmatrix} \oplus \begin{pmatrix} 0 & 0 \\ 0 & 0 \end{pmatrix}, \quad (11)$$

where the 6×6 matrix consists of two zero modes coupled with a free Dirac fermion. Then it is straightforward to check that the eigenvalues of this 6×6 matrix has two zero modes, so that the entire system has four zero modes, leading to double flat bands. For $A-ABC-A$, the simplified $\mathbf{k} \cdot \mathbf{p}$ model can be written in a similar form

$$H_{A-ABC-A} = \begin{pmatrix} 0 & \tilde{h}_+ & 0 \\ \tilde{h}_- & h(\mathbf{k}) & \tilde{h}_+ \\ 0 & \tilde{h}_- & 0 \end{pmatrix} \oplus \begin{pmatrix} 0 & 0 \\ 0 & 0 \end{pmatrix} \quad (12)$$

Due to the change of stacking chirality, the 6×6 Hamiltonian consisting of two zero modes coupled with a free Dirac fermion no longer has zero-mode solution. Thus, there are only two zero modes for the $A-ABC-A$ system, contributing to one pair of flat bands per spin per valley.

We can generalize the above argument for $L > 3$ and $M, N > 1$. According to the partition rules, the number of chiral segments in the L multilayers have a dramatic influence on the number of flat bands, while the segments in the M and N multilayers do not. First, if the middle L multilayers has a chiral stacking, i.e., $S_L = 1$, then the system is equivalent to the $A-ABC-A$ system with a renormalized interlayer hopping parameter between untwisted layers t'_{\perp} . As a result, there is only one pair of flat bands (in the chiral limit) for the middle L layers with chiral stacking. Second, if the L multilayers can be decomposed into two segments ($S_L = 2$), the corresponding simplified $\mathbf{k} \cdot \mathbf{p}$ model is equivalent to that of the $A-ABA-A$ system with renormalized hopping parameters, which has double flat bands. Finally, for $S_L > 2$: we can argue that for alternating twist multilayers, two pairs of moiré potentials are coupled together through several chiral segments within the L multilayers, so that the more the segments are, the weaker the couple is. As a result, we can treat them as nearly decoupled and there are four flat bands for the $S_L > 2$ situation. Therefore, if the middle L multilayers has $S_L > 1$, there would be double flat bands for each spin and valley degrees of freedom.

It is worthwhile to note that the simplified $\mathbf{k} \cdot \mathbf{p}$ model is constructed in the chiral limit neglecting all the intrasublattice couplings. Consequently, the partition rules derived from the simplified $\mathbf{k} \cdot \mathbf{p}$ model and the above discussions about double flat bands are rigorous only in the chiral limit. In a more realistic situation, one needs to include the intrasublattice component of the moiré potential and the further neighbor interlayer hoppings within the untwisted layers as in Eq. (23), which break chiral symmetry. With these additional coupling terms, the

otherwise exactly flat bands at the magic angle may acquire nonzero bandwidths, and the $E(\mathbf{k}) \sim k^J$ bands may have slightly modified dispersion. However, despite these perturbative changes, the main conclusions sketched by the partition rules are unchanged.

It follows from the previous arguments that a mirror-symmetric ATMG system with $L > 1$ must satisfy the condition of $S_L > 1$, thus there must be two pairs of flat bands. The double flat bands can be classified by the opposite mirror eigenvalues ± 1 for ATMG with m_z symmetry⁷³. In Fig. 3(a) we present the band structures of the *A-ABA-A* system including the intrasublattice moiré potential and the further neighbor interlayer hopping, where the color coding indicates the weight projected onto the middle layer. First, we note that compared with the band structures in the chiral limit shown Fig. 1(d), in the realistic situation two of the four flat bands become more dispersive with the bandwidth ~ 25 meV, while the other pair of flat bands remain flat with very small bandwidth ~ 10 meV. Second, we note that the weight of the middle layer for the pair of flat bands lower in energy with small bandwidth is vanishing, while the upper pair of flat bands with relatively large bandwidth have significant contributions from the middle-layer states. This is because the two flat bands lower/upper in energy have mirror eigenvalues ∓ 1 , and the Bloch states with -1 mirror eigenvalue must have zero contribution from the middle layer. In the presence of Coulomb interactions, the m_z symmetry could be broken spontaneously at certain filling factors.

V. CORRELATION EFFECTS IN MIRROR-SYMMETRIC ATMG SYSTEM

The ubiquitous flat bands in ATMG make these systems strongly susceptible to Coulomb interactions. Moreover, unlike magic-angle TBG, in magic-angle ATMG typically there are flat bands co-existing with other dispersive bands (such as Dirac cone) or double flat bands in these systems. The extra low-energy dispersive bands (e.g., Dirac cone) may be coupled with the flat bands under weak displacement fields and display different correlated states from those in magic-angle TBG at certain filling factors^{75,76}. On the other hand, in mirror-symmetric ATMG with double flat bands, e.g., in *A-ABA-A* system, the extra pair of flat bands marked by opposite mirror eigenvalues introduce additional degrees of freedom. What are the correlated ground states in such double-flat-band systems at different filling factors of the flat bands, how the extra degrees of freedom (mirror eigenvalues) would play a role, and how the correlated states would differ from those of TBG, are all open questions. We try to answer these questions by studying the correlated states at different integer fillings of ATMG with *A-ABA-A* stacking, the simplest mirror-symmetric ATMG system with double flat bands.

A. Symmetry-breaking ground states

We have performed unrestricted self-consistent Hartree-Fock calculations for the *A-ABA-A* system within the subspace of the double flat bands. In particular, the intersite Coulomb interactions in graphene-based systems can be written as

$$H_C = \frac{1}{2N_s} \sum_{\alpha\alpha'} \sum_{\mathbf{k}_a\mathbf{k}'_a\mathbf{q}_a} \sum_{\sigma\sigma'} V(\mathbf{q}_a) \times \hat{c}_{\mathbf{k}_a+\mathbf{q}_a,\alpha\sigma}^\dagger \hat{c}_{\mathbf{k}'_a-\mathbf{q}_a,\alpha'\sigma'}^\dagger \hat{c}_{\mathbf{k}'_a,\alpha'\sigma'} \hat{c}_{\mathbf{k}_a,\alpha\sigma} \quad (13)$$

where N_s is the total number of moiré cells in the system, $\mathbf{k}_a, \mathbf{k}'_a, \mathbf{q}_a$ are the atomic wavevectors of graphene, α, α' denote the layer and sublattice indices, and σ is the spin index. If one expands the wavevector around the Dirac points \mathbf{K} and \mathbf{K}' , the Coulomb interaction can be further decomposed into the intravalley part and the intervalley part, with the former interaction strength being two orders of magnitudes greater than the latter for small twist angles $\theta \sim 1^\circ$. Therefore, we only consider the intravalley Coulomb interactions in this work, which is expressed as

$$H_C^{\text{intra}} = \frac{1}{2N_s} \sum_{\mathbf{k}_a\mathbf{k}'_a\mathbf{q}_a} \sum_{\mu\mu',\sigma\sigma',\alpha\alpha'} V(\mathbf{q}_a) \hat{c}_{\mathbf{k}_a+\mathbf{q}_a,\mu\alpha\sigma}^\dagger \hat{c}_{\mathbf{k}'_a-\mathbf{q}_a,\mu'\alpha'\sigma'}^\dagger \times \hat{c}_{\mathbf{k}'_a,\mu'\alpha'\sigma'} \hat{c}_{\mathbf{k}_a,\mu\alpha\sigma} \quad (14)$$

where $\mu, \mu' = \pm$ are the valley indices, and now the wavevectors \mathbf{k}, \mathbf{k}' , and \mathbf{q} are expanded around the Dirac point of valley μ (\mathbf{K}^μ), which can be decomposed as $\mathbf{k}_a = \mathbf{k} + \mathbf{Q}$, where \mathbf{k} is the moiré wavevector in moiré Brillouin zone, and \mathbf{Q} is the moiré lattice vector. A single-gate screened Coulomb interaction $V(\mathbf{q}_a) = e^2(1 - e^{-2|\mathbf{q}_a|d_s})/(2\Omega_M\epsilon_{\text{BN}}|\mathbf{q}_a|)$ is adopted in this work, where Ω_M is the area of moiré primitive cell, $d_s = 40$ nm is the distance between ATMG layers and the metallic gate, $\epsilon_{\text{BN}} \approx 4$ is the dielectric constant of the BN substrate. The Coulomb interactions are further projected onto the double flat bands, and we perform self-consistent Hartree-Fock calculations within the subspace of the double flat bands. Besides, the Coulomb interactions between electrons in flat bands can be further screened by remote-band particle-hole excitation, and such screening effects in our calculation are treated with the constrained random phase approximation (cRPA)⁴⁰, where the cRPA dielectric constant $\epsilon(\mathbf{q} + \mathbf{Q}) = \epsilon_{\text{BN}}(\mathbb{1} + \hat{\chi}^0(\mathbf{q})\hat{V}(\mathbf{q}))_{\mathbf{Q},\mathbf{Q}}$, where $\hat{\chi}^0(\mathbf{q})$ is the zero-frequency bare susceptibility at moiré wavevector \mathbf{q} , and $\hat{V}(\mathbf{q})$ is the Coulomb interaction matrix defined in the space of reciprocal moiré lattice vector \mathbf{Q} , with $\hat{V}(\mathbf{q})_{\mathbf{Q},\mathbf{Q}} = V(\mathbf{q} + \mathbf{Q})$. We refer the readers to Supplementary Information (Appendix III-IV) for more details about the Hartree-Fock and cRPA formalism.

To start with, we calculate the ground states at different integer fillings of the double flat bands using the Hartree-Fock and cRPA methods described above. The filling factor is counted with respect to the CNP, i.e., the filling factor is defined as $\nu = n - 8$ when n out of

TABLE II: Gap, main order parameter, polarization and valley polarization of the Hartree-Fock ground states at different filling factor. The unit of polarization is $e \cdot \text{\AA}$ per moiré supercell. The unit of valley polarization is charge per unit cell.

filling factor	gap(eV)	main order parameter	polarization	valley polarization
-7	0.0119	$s_z \tau_0 \sigma_0$	-0.0103	0.398
-6	0.0208	$s_z \tau_0 \sigma_0$	-0.0009	0.048
-5	0.0132	$s_z \tau_0 \sigma_0, s_0 \tau_z \sigma_0$	-0.0110	0.624
-4	/	$s_z \tau_0 \sigma_0$	0.0197	-1.179
-3	0.0148	$s_z \tau_0, z \sigma_0$	-0.0112	-0.406
-2	/	$s_0 \tau_z \sigma_0$	0.0732	-1.364
-1	0.0073	$s_0 \tau_z \sigma_0$	0.0585	-3.046
0	/	$s_0 \tau_x \sigma_y$	0.1004	0.014
1	/	$s_0 \tau_z \sigma_0$	0.0708	-2.705
2	0.0095	$s_z \tau_0 \sigma_0$	0.0834	-0.030
3	0.0063	$s_{0,z} \tau_{0,z} \sigma_0$	0.0713	1.000
4	0.0131	$s_0 \tau_0 \sigma_0$	0.0834	0.000
5	/	$s_{0,z} \tau_{0,z} \sigma_0$	0.0771	-0.988
6	/	$s_0 \tau_z \sigma_0$	0.0741	-1.963
7	/	$s_{0,z} \tau_{0,z} \sigma_0$	0.0264	-0.967

the 16 flat bands (including valley and spin degeneracy) are filled. Then we calculate the expectation values of the order parameters of the Hartree-Fock ground states at each integer filling, and figure out the dominant ones which are presented in Table II, where τ , s , and σ denote Pauli matrices defined in valley, spin, and sublattice space respectively. For example, the ground state at filling -3 is a gaped spin-valley polarized state. In order to depict the spontaneous m_z symmetry breaking, we also calculate the vertical electric polarization at different filling factors. The vertical electric polarization per moiré supercell p_z is defined as: $p_z = \sum_{l=1}^5 (l-3) q_l d_0$, where $d_0 = 3.35 \text{\AA}$ is the interlayer distance of Bernal bilayer graphene, $q_l = e \langle \tau_0 s_0 \mathbb{L}_l \sigma_0 \rangle$ is the layer resolved charge density, where \mathbb{L}_l is the projection operator onto layer l , a 5×5 matrix with the l th diagonal element identity and all other elements being zeros. The unit of the electric polarization is $e \cdot \text{\AA}$ per moiré supercell. We also evaluate the orbital magnetization and valley polarization. The valley polarization ξ_z is defined as: $\xi_z = \sum_{l=1}^5 \xi_z(l) = \sum_{l=1}^5 \langle \tau_z s_0 \mathbb{L}_l \sigma_0 \rangle$, where $\langle \tau_z(l) \rangle$ is defined as the valley polarization projected onto layer l . A finite valley polarization would split the two valleys and would give rise to nonzero net orbital magnetization. In Table II, we present the calculated vertical electric polarization and valley polarization of the spontaneous symmetry-breaking states at different filling factors. We find that m_z symmetry is spontaneously broken by Coulomb interactions at all integer fillings, which generate small but nonzero electric polarization.

B. Orbital magnetoelectric effect through intertwined orders

To characterize the effect of vertical electric field, we calculate both the vertical electric polarization and valley polarization of the Hartree-Fock ground states for the $A - ABA - A$ system at filling factor -3 with increasing

displacement fields. The displacement field (D) is introduced by applying a homogeneous vertical electrostatic potential difference U_d between the topmost and bottommost layer, i.e., $U_d = e D d_0 \times 4 / \epsilon_{\text{BN}}$, where $\epsilon_{\text{BN}} \approx 4$ is the dielectric constant of the BN substrate. Our calculations indicate that the dominant order parameters of the ground states at filling -3 are unchanged under different U_d , i.e., the system always stays in the spin-valley polarized state with broken m_z symmetry, suggesting that the no phase transition occurs at least for $0 \leq U_d \leq 0.02 \text{ eV}$. However, by virtue of the m_z symmetry and the additional layer degrees of freedom, the valley polarization acquires nontrivial layer distributions as shown by the $\xi_z(l)$ ($l = 1, \dots, 5$) values in Table III. We see that $\xi_z(1)$ and $\xi_z(2)$ are approximately the same, while $\xi_z(4)$ and $\xi_z(5)$ are approximately the same, which are different from $\xi_z(3)$. As a result, the layer-resolved valley polarization can be approximately decomposed into three terms:

$$\hat{\xi}_z \approx \xi_z^s \mathbb{1}_{5 \times 5} + \xi_z^a \hat{P}_z + \xi_z^a \hat{Q}_z \quad (15)$$

where

$$\hat{P}_z = \begin{pmatrix} -2 & 0 & 0 & 0 & 0 \\ 0 & -1 & 0 & 0 & 0 \\ 0 & 0 & 0 & 0 & 0 \\ 0 & 0 & 0 & 1 & 0 \\ 0 & 0 & 0 & 0 & 2 \end{pmatrix}, \quad \hat{Q}_z = \begin{pmatrix} 1 & 0 & 0 & 0 & 0 \\ 0 & 0 & 0 & 0 & 0 \\ 0 & 0 & 0 & 0 & 0 \\ 0 & 0 & 0 & 0 & 0 \\ 0 & 0 & 0 & 0 & -1 \end{pmatrix} \quad (16)$$

and $\hat{\xi}_z$ is a 5×5 matrix with its l th diagonal element denoting the valley polarization contributed by layer l ,

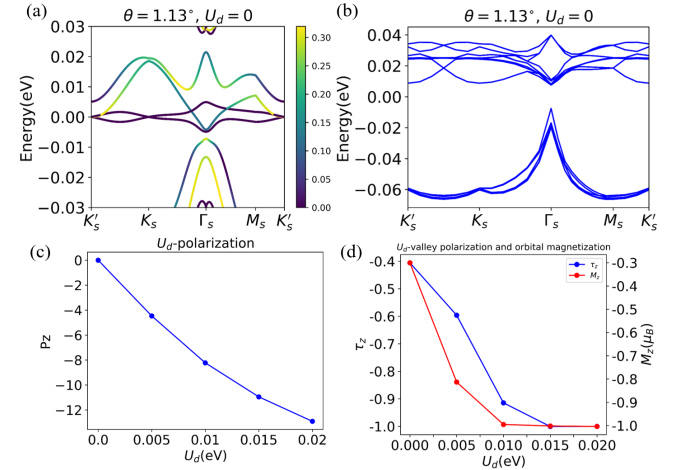


FIG. 3: The band structure of $A - ABA - A$ for two valleys including intrasublattice moiré potential and the further neighbor interlayer hopping. (a) The non-interacting band structures with weight projected to the middlemost layer. (b) The Hartree-Fock band structure for two valleys. (c) The vertical polarization, and (d) the valley polarization and the corresponding orbital magnetization of the symmetry-breaking ground state at -3 filling as a function of vertical electrostatic potential drop U_d .

i.e., $\hat{\xi}_{z,l} = \xi_z(l)$. ξ_z^s and ξ_z^a denote the layer-symmetric and layer anti-symmetric components of the valley polarization, with $\xi_z^s = \sum_{l=1}^5 \xi_z(l)/5$, and $\xi_z^a = \sum_{l \neq 3} \text{sgn}[(l-3)](\xi_z(l) - \xi_z^s)/4$. In other words, $\xi_z^s = \langle \tau_z \otimes \mathbb{1}_{5 \times 5} \rangle / 5$ is the layer average of valley polarization ($\mathbb{1}_{5 \times 5}$ denotes identity matrix in layer space), and $\xi_z^a = \langle \tau_z \otimes (\hat{P}_z + \hat{Q}_z) \rangle / 4$, where $\langle \hat{O} \rangle$ denotes the expectation value of operator \hat{O} evaluated with respect to the symmetry-breaking ground state. The layer-symmetric and layer anti-symmetric valley polarization for the ground states at filling -3 with different U_d are presented in the last two rows of Table III.

We note that \hat{P}_z is exactly the vertical electric polarization operator $\hat{p}_z = ed_0 \hat{P}_z$, which couples linearly to external electric field; while the valley polarization operator is proportional to the orbital magnetization operator $\hat{M}_z = g_z \mu_B \tau_z$ which couples linearly to external magnetic field, where g_z is introduced as an effective g factor and μ_B is the Bohr magneton. Given the above discussions, we introduce an effective mean-field Hamiltonian to describe how the symmetry-breaking state at filling -3 would respond to external electric and magnetic fields

$$H(\mathbf{k}) = H_0(\mathbf{k}) + \Delta_{z0} \tau_z \otimes \mathbb{1}_{5 \times 5} + \Delta_{zz} \tau_z \otimes (\hat{P}_z + \hat{Q}_z) - g_z \mu_B B_z \tau_z \otimes \mathbb{1}_{5 \times 5} + \frac{1}{4} U_d \tau_0 \otimes \hat{P}_z, \quad (17)$$

where Δ_{z0} and Δ_{zz} are the “mean fields” that are self consistently generated by Coulomb interactions which are coupled with the $\tau_z \otimes \mathbb{1}_{5 \times 5}$ operator and $\tau_z \otimes (\hat{P}_z + \hat{Q}_z)$ operator respectively, while B_z is the vertical magnetic field and U_d is the vertical electrostatic energy drop. As the electric polarization operator and the valley polarization operator are intertwined together, Eq. (17) implies a tunable electric polarization by magnetic field and conversely a tunable valley polarization (orbital magnetization) by electric field. To be specific, a vertical electric field is coupled to the \hat{P}_z operator, which is in turn intertwined with the layer anti-symmetric component of the valley polarization operator, thus would change the valley polarization and orbital magnetization of the system. Conversely, a vertical magnetic B_z is coupled to orbital magnetization (valley polarization), and the valley polarization operator is intertwined with the electric polarization operator, which would change electric polarization of the system. It is clearly seen from Table III that the layer symmetric valley polarization is larger than the layer anti-symmetric one, implying that the orbital magnetization still has the strongest coupling to magnetic field, but can tuned by electric field. In Fig. 3(c) and (d), we present the calculated electric polarization and valley polarization of the symmetry-breaking states at filling -3 under different U_d . As U_d increases, clearly the electric polarization is linearly enhanced as shown in Fig. 3(c). On the other hand, the valley polarization and the corresponding orbital magnetization are also dramatically

TABLE III: Layer resolved valley polarization for the ground states at filling -3 under different U_d . $\xi_z^s = \sum_{l=1}^5 \xi_z(l)/5$, and $\xi_z^a = \sum_{l \neq 3} \text{sgn}[(l-3)](\xi_z(l) - \xi_z^s)/4$.

U_d (eV)	0	0.005	0.010	0.015	0.020
$\xi_z(1)$	-0.0994	-0.1690	-0.2556	-0.2724	-0.2792
$\xi_z(2)$	-0.0996	-0.1676	-0.2547	-0.2720	-0.2780
$\xi_z(3)$	-0.0065	0.0023	-0.0685	-0.1317	-0.1469
$\xi_z(4)$	-0.1003	-0.1309	-0.1683	-0.1626	-0.1482
$\xi_z(5)$	-0.1000	-0.1309	-0.1674	-0.1617	-0.1477
ξ_z^s	-0.0998	-0.1496	-0.2115	-0.2172	-0.2133
ξ_z^a	0.0003	0.0187	0.0437	0.0550	0.0653

enhanced with the increase of U_d as shown by the blue and red dots in Fig. 3(d). This indicates a novel type of orbital magnetoelectric effect driven by Coulomb interactions in mirror-symmetric ATMG system with double flat bands.

To summarize, in this work we have theoretically studied the electronic structures and interaction effects of alternating twisted multilayer graphene (ATMG) systems. We find that these ATMG systems exhibit various intriguing non-interacting band dispersion including one pair of flat bands, one pair of flat bands co-existing with Dirac cones or more generally $E(\mathbf{k}) \sim k^J$ (J is positive integer) dispersion, as well as two pairs of flat bands which may also co-exist with $E(\mathbf{k}) \sim k^J$ (J is positive integer) dispersion. Based on an analytic analysis from a simplified $\mathbf{k} \cdot \mathbf{p}$ model approach, we find that the low energy band structure can be described by a set of generic partition rules. We have also considered Coulomb interaction effects in ATMG with $A - ABA - A$ stacking, the simplest mirror symmetric ATMG system having two pairs of flat bands. We have studied the symmetry-breaking ground states at different integer filling factors under zero external fields based on unrestricted Hartree-Fock calculations. We find that at certain fillings both time-reversal symmetry and the mirror symmetry can be broken spontaneously by Coulomb interactions, leading to insulator states with intertwined electric polarization and orbital magnetization. As a result of such intertwined ordering, the system can exhibit a novel type of orbital magnetoelectric effect with the orbital magnetization (electric polarization) being highly tunable by external electric (magnetic) field. Our work is a significant step forward in understanding the electronic structures and correlation effects of alternating twisted graphene systems, and will provide useful guidelines for future experimental and theoretical studies.

Acknowledgments

This work is supported by the National Key R & D program of China (grant no. 2020YFA0309601), the National Science Foundation of China (grant no. 12174257), and the start-up grant of ShanghaiTech University.

- ¹ Y. Cao, V. Fatemi, S. Fang, K. Watanabe, T. Taniguchi, E. Kaxiras, and P. Jarillo-Herrero, *Nature* **556**, 43 (2018).
- ² M. Yankowitz, S. Chen, H. Polshyn, Y. Zhang, K. Watanabe, T. Taniguchi, D. Graf, A. F. Young, and C. R. Dean, *Science* **363**, 1059 (2019).
- ³ E. Codecido, Q. Wang, R. Koester, S. Che, H. Tian, R. Lv, S. Tran, K. Watanabe, T. Taniguchi, F. Zhang, et al., *Science Advances* **5** (2019).
- ⁴ X. Lu, P. Stepanov, W. Yang, M. Xie, M. A. Aamir, I. Das, C. Urgell, K. Watanabe, T. Taniguchi, G. Zhang, et al., *Nature* **574**, 653 (2019), ISSN 14764687, URL <http://dx.doi.org/10.1038/s41586-019-1695-0>.
- ⁵ P. Stepanov, I. Das, X. Lu, A. Fahimniya, K. Watanabe, T. Taniguchi, F. H. L. Koppens, J. Lischner, L. Levitov, and D. K. Efetov, *Nature* **583**, 375 (2020), ISSN 1476-4687.
- ⁶ Y. Saito, J. Ge, K. Watanabe, T. Taniguchi, and A. F. Young, *Nature Physics* **16**, 926 (2020), ISSN 1745-2481.
- ⁷ X. Liu, Z. Wang, K. Watanabe, T. Taniguchi, O. Vafek, and J. Li, *Science* **371**, 1261 (2021).
- ⁸ Y. Cao, D. Rodan-Legrain, J. M. Park, N. F. Yuan, K. Watanabe, T. Taniguchi, R. M. Fernandes, L. Fu, and P. Jarillo-Herrero, *science* **372**, 264 (2021).
- ⁹ M. Serlin, C. L. Tschirhart, H. Polshyn, Y. Zhang, J. Zhu, K. Watanabe, T. Taniguchi, L. Balents, and A. F. Young, *Science* (2019), ISSN 0036-8075, URL <https://www.sciencemag.org/lookup/doi/10.1126/science.aay5533>.
- ¹⁰ A. L. Sharpe, E. J. Fox, A. W. Barnard, J. Finney, K. Watanabe, T. Taniguchi, M. A. Kastner, and D. Goldhaber-Gordon, *science* **365**, 605 (2019).
- ¹¹ P. Stepanov, M. Xie, T. Taniguchi, K. Watanabe, X. Lu, A. H. MacDonald, B. A. Bernevig, and D. K. Efetov (2020), 2012.15126.
- ¹² K. P. Nuckolls, M. Oh, D. Wong, B. Lian, K. Watanabe, T. Taniguchi, B. A. Bernevig, and A. Yazdani, *Nature* **588**, 610 (2020).
- ¹³ S. Wu, Z. Zhang, K. Watanabe, T. Taniguchi, and E. Y. Andrei, *Nature Materials* (2021), ISSN 1476-4660.
- ¹⁴ I. Das, X. Lu, J. Herzog-Arbeitman, Z.-D. Song, K. Watanabe, T. Taniguchi, B. A. Bernevig, and D. K. Efetov, *Nature Physics* **17**, 710 (2021).
- ¹⁵ A. T. Pierce, Y. Xie, J. M. Park, E. Khalaf, S. H. Lee, Y. Cao, D. E. Parker, P. R. Forrester, S. Chen, K. Watanabe, et al. (2021), 2101.04123.
- ¹⁶ C. Shen, Y. Chu, Q. Wu, N. Li, S. Wang, Y. Zhao, J. Tang, J. Liu, J. Tian, K. Watanabe, et al., *Nature Physics* **16**, 520 (2020), ISSN 1745-2473, URL <http://www.nature.com/articles/s41567-020-0825-9>.
- ¹⁷ Y. Cao, V. Fatemi, A. Demir, S. Fang, S. L. Tomarken, J. Y. Luo, J. D. Sanchez-Yamagishi, K. Watanabe, T. Taniguchi, E. Kaxiras, et al., *Nature* **556**, 80 (2018), URL <http://dx.doi.org/10.1038/nature26154>.
- ¹⁸ A. Kerelsky, L. J. McGilly, D. M. Kennes, L. Xian, M. Yankowitz, S. Chen, K. Watanabe, T. Taniguchi, J. Hone, C. Dean, et al., *Nature* **572**, 95 (2019).
- ¹⁹ Y. Jiang, X. Lai, K. Watanabe, T. Taniguchi, K. Haule, J. Mao, and E. Y. Andrei, *Nature (London)* **573**, 91 (2019).
- ²⁰ Y. Xie, B. Lian, B. Jäck, X. Liu, C.-L. Chiu, K. Watanabe, T. Taniguchi, B. A. Bernevig, and A. Yazdani, *Nature (London)* **572**, 101 (2019).
- ²¹ Y. Choi, J. Kemmer, Y. Peng, A. Thomson, H. Arora, R. Polski, Y. Zhang, H. Ren, J. Alicea, G. Refael, et al., *Nature Physics* pp. 1–7 (2019).
- ²² R. Bistritzer and A. H. MacDonald, *Proceedings of the National Academy of Sciences* **108**, 12233 (2011).
- ²³ G. Tarnopolsky, A. J. Kruchkov, and A. Vishwanath, *Phys. Rev. Lett.* **122**, 106405 (2019), URL <https://link.aps.org/doi/10.1103/PhysRevLett.122.106405>.
- ²⁴ J. Liu, J. Liu, and X. Dai, *Phys. Rev. B* **99**, 155415 (2019), URL <https://link.aps.org/doi/10.1103/PhysRevB.99.155415>.
- ²⁵ Z. Song, Z. Wang, W. Shi, G. Li, C. Fang, and B. A. Bernevig, *Phys. Rev. Lett.* **123**, 036401 (2019), ISSN 0031-9007, URL <http://dx.doi.org/10.1103/PhysRevLett.123.036401>.
- ²⁶ J. Ahn, S. Park, and B.-J. Yang, *Phys. Rev. X* **9**, 021013 (2019).
- ²⁷ H. C. Po, L. Zou, T. Senthil, and A. Vishwanath, *Phys. Rev. B* **99**, 195455 (2019).
- ²⁸ P. J. Ledwith, G. Tarnopolsky, E. Khalaf, and A. Vishwanath, *Phys. Rev. Research* **2**, 023237 (2020).
- ²⁹ L. Balents, C. R. Dean, D. K. Efetov, and A. F. Young, *Nature Physics* **16**, 725 (2020), ISSN 1745-2481.
- ³⁰ E. Y. Andrei, D. K. Efetov, P. Jarillo-Herrero, A. H. MacDonald, K. F. Mak, T. Senthil, E. Tutuc, A. Yazdani, and A. F. Young, *Nature Reviews Materials* **6**, 201 (2021), ISSN 2058-8437.
- ³¹ J. Liu and X. Dai, *Nature Reviews Physics* **3**, 367 (2021), ISSN 2522-5820.
- ³² J. Kang and O. Vafek, *Phys. Rev. Lett.* **122**, 246401 (2019).
- ³³ K. Seo, V. N. Kotov, and B. Uchoa, *Phys. Rev. Lett.* **122**, 246402 (2019).
- ³⁴ M. Xie and A. H. MacDonald, *Phys. Rev. Lett.* **124**, 097601 (2020).
- ³⁵ F. Wu, *Phys. Rev. B* **99**, 195114 (2019).
- ³⁶ N. Bultinck, S. Chatterjee, and M. P. Zaletel, *Phys. Rev. Lett.* **124**, 166601 (2020).
- ³⁷ F. Wu and S. Das Sarma, *Phys. Rev. Lett.* **124**, 046403 (2020).
- ³⁸ N. Bultinck, E. Khalaf, S. Liu, S. Chatterjee, A. Vishwanath, and M. P. Zaletel, *Phys. Rev. X* **10**, 031034 (2020).
- ³⁹ J. Liu and X. Dai, *Phys. Rev. B* **103**, 035427 (2021).
- ⁴⁰ S. Zhang, X. Lu, and J. Liu (2021), 2109.11441.
- ⁴¹ K. Hejazi, X. Chen, and L. Balents, *Phys. Rev. Research* **3**, 013242 (2021).
- ⁴² J. Kang and O. Vafek, *Phys. Rev. B* **102**, 035161 (2020).
- ⁴³ B.-B. Chen, Y. D. Liao, Z. Chen, O. Vafek, J. Kang, W. Li, and Z. Y. Meng, *Nature Communications* **12**, 5480 (2021).
- ⁴⁴ C. Lu, Y. Zhang, Y. Zhang, M. Zhang, C.-C. Liu, Z.-C. Gu, W.-Q. Chen, and F. Yang, *arXiv preprint arXiv:2003.09513* (2020).
- ⁴⁵ Y. Da Liao, J. Kang, C. N. Breiø, X. Y. Xu, H.-Q. Wu, B. M. Andersen, R. M. Fernandes, and Z. Y. Meng, *Phys. Rev. X* **11**, 011014 (2021).
- ⁴⁶ B. A. Bernevig, Z.-D. Song, N. Regnault, and B. Lian, *arXiv preprint arXiv:2009.12376* (2020).
- ⁴⁷ B. Lian, Z.-D. Song, N. Regnault, D. K. Efetov, A. Yazdani, and B. A. Bernevig, *arXiv preprint arXiv:2009.13530* (2020).
- ⁴⁸ F. Xie, A. Cowsik, Z.-D. Song, B. Lian, B. A. Bernevig, and N. Regnault, *Phys. Rev. B* **103**, 205416 (2021).

- ⁴⁹ T. Soejima, D. E. Parker, N. Bultinck, J. Hauschild, and M. P. Zaletel, *Phys. Rev. B* **102**, 205111 (2020).
- ⁵⁰ P. Potasz, M. Xie, and A. H. MacDonald (2021), 2102.02256.
- ⁵¹ X. Zhang, G. Pan, Y. Zhang, J. Kang, and Z. Y. Meng, *Chinese Physics Letters* **38**, 077305 (2021).
- ⁵² J. S. Hofmann, E. Khalaf, A. Vishwanath, E. Berg, and J. Y. Lee (2021), 2105.12112.
- ⁵³ D. E. Parker, T. Soejima, J. Hauschild, M. P. Zaletel, and N. Bultinck, *Phys. Rev. Lett.* **127**, 027601 (2021).
- ⁵⁴ W.-Y. He, D. Goldhaber-Gordon, and K. T. Law, *Nature Communications* **11**, 1650 (2020).
- ⁵⁵ J. Zhu, J.-J. Su, and A. H. MacDonald, *Phys. Rev. Lett.* **125**, 227702 (2020).
- ⁵⁶ C. Huang, N. Wei, and A. H. MacDonald, *Phys. Rev. Lett.* **126**, 056801 (2021).
- ⁵⁷ X. Ying, M. Ye, and L. Balents, *Phys. Rev. B* **103**, 115436 (2021).
- ⁵⁸ J. Liu, Z. Ma, J. Gao, and X. Dai, *Phys. Rev. X* **9**, 031021 (2019), URL <https://link.aps.org/doi/10.1103/PhysRevX.9.031021>.
- ⁵⁹ J. Y. Lee, E. Khalaf, S. Liu, X. Liu, Z. Hao, P. Kim, and A. Vishwanath, *Nature Communications* **10**, 5333 (2019).
- ⁶⁰ M. Koshino, *Phys. Rev. B* **99**, 235406 (2019), URL <https://link.aps.org/doi/10.1103/PhysRevB.99.235406>.
- ⁶¹ X. Liu, Z. Hao, E. Khalaf, J. Y. Lee, Y. Ronen, H. Yoo, D. Haei Najafabadi, K. Watanabe, T. Taniguchi, A. Vishwanath, et al., *Nature* **583**, 221 (2020).
- ⁶² Y. Cao, D. Rodan-Legrain, O. Rubies-Bigorda, J. M. Park, K. Watanabe, T. Taniguchi, and P. Jarillo-Herrero, *Nature* (2020), ISSN 1476-4687.
- ⁶³ H. Polshyn, J. Zhu, M. Kumar, Y. Zhang, F. Yang, C. Tschirhart, M. Serlin, K. Watanabe, T. Taniguchi, A. MacDonald, et al., *Nature* pp. 1–5 (2020).
- ⁶⁴ S. Chen, M. He, Y.-H. Zhang, V. Hsieh, Z. Fei, K. Watanabe, T. Taniguchi, D. H. Cobden, X. Xu, C. R. Dean, et al., *Nat. Phys.* (2020).
- ⁶⁵ M. He, Y. Li, J. Cai, Y. Liu, K. Watanabe, T. Taniguchi, X. Xu, and M. Yankowitz, *Nat. Phys.* (2020).
- ⁶⁶ S. Xu, M. M. Al Ezzi, N. Balakrishnan, A. Garcia-Ruiz, B. Tsim, C. Mullan, J. Barrier, N. Xin, B. A. Piot, T. Taniguchi, et al., *Nature Physics* **17**, 619 (2021).
- ⁶⁷ Z. Ma, S. Li, M. Lu, D.-H. Xu, J.-H. Gao, and X. C. Xie (2021), 2104.06860.
- ⁶⁸ H. Kim, Y. Choi, C. Lewandowski, A. Thomson, Y. Zhang, R. Polski, K. Watanabe, T. Taniguchi, J. Alicea, and S. Nadj-Perge (2021), 2109.12127.
- ⁶⁹ Y. Cao, J. M. Park, K. Watanabe, T. Taniguchi, and P. Jarillo-Herrero, *Nature* **595**, 526 (2021).
- ⁷⁰ J. M. Park, Y. Cao, K. Watanabe, T. Taniguchi, and P. Jarillo-Herrero, *Nature* **590**, 249 (2021).
- ⁷¹ X. Liu, K. Watanabe, T. Taniguchi, and J. Li, arXiv preprint arXiv:2108.03338 (2021).
- ⁷² E. Khalaf, A. J. Kruchkov, G. Tarnopolsky, and A. Vishwanath, *Phys. Rev. B* **100**, 085109 (2019), URL <https://link.aps.org/doi/10.1103/PhysRevB.100.085109>.
- ⁷³ X. Li, F. Wu, and A. H. MacDonald (2019), 1907.12338.
- ⁷⁴ M. Christos, S. Sachdev, and M. S. Scheurer (2021), 2106.02063.
- ⁷⁵ F. Xie, N. Regnault, D. Călugăru, B. A. Bernevig, and B. Lian, *Physical Review B* **104**, 115167 (2021).
- ⁷⁶ D. Călugăru, F. Xie, Z.-D. Song, B. Lian, N. Regnault, and B. A. Bernevig, *Phys. Rev. B* **103**, 195411 (2021).
- ⁷⁷ S. Zhang, B. Xie, Q. Wu, J. Liu, and O. V. Yazyev (2020), 2012.11964.
- ⁷⁸ M. Koshino, N. F. Q. Yuan, T. Koretsune, M. Ochi, K. Kuroki, and L. Fu, *Phys. Rev. X* **8**, 031087 (2018).
- ⁷⁹ S. Zhang and J. Liu (2021), 2101.04711.

Supplementary Information

I The lattice structure and continuum model for alternating twisted multilayer graphene

The moiré pattern is formed by a small twist angle θ between two layers, where $\cos(\theta) = (3m^2 + 3m + 1/2)/(3m^2 + 3m + 1)$. The lattice vectors of the moiré supercell are: $\mathbf{t}_1 = (\sqrt{3}/2, 1/2) \cdot L_s$, $\mathbf{t}_2 = (0, 1) \cdot L_s$, where $L_s = a/(2 \sin(\theta/2))$ is the moiré lattice constant, a is the atomic lattice constant of graphene. We consider corrugation between twisted layers for $L > 1$, modeled as⁷⁸:

$$d_z(\mathbf{r}) = d_0 + 2d_1 \sum_{j=1}^3 \cos(\mathbf{b}_j \cdot \delta(\mathbf{r})) \quad (18)$$

where $\mathbf{b}_1 = (1, 1/\sqrt{3}) \cdot 2\pi/a$, $\mathbf{b}_2 = (-1, 1/\sqrt{3}) \cdot 2\pi/a$, $\mathbf{b}_3 = (0, 2) \cdot 2\pi/a$. $\delta(\mathbf{r})$ is the local shift between two carbon atoms. $d_0 = 3.433 \text{ \AA}$, $d_1 = 0.0278 \text{ \AA}$. For $L=1$:

$$\begin{aligned} d_{z,twist}(\mathbf{r}) &= d_0 + 2d_1 \sum_{j=1}^3 \cos(\mathbf{b}_j \cdot \delta(\mathbf{r})) \\ d_{z,untwist}(\mathbf{r}) &= d_{AB} + d_{AA}/2 - d_{z,twist}(\mathbf{r}) \end{aligned} \quad (19)$$

In this situation, the middle layer can be treated as ideally flat, so that it will not break m_z symmetry. The corrugation difference does not matter to continuum model.

The low-energy electronic structure of ATMG can be well described based on the Bistritzer-MacDonald continuum model²². The free Dirac fermions from the atomic K and K' valleys contribute to the low energy states of ATMG. We can treat low energy states from two different atomic valleys as decoupled at the non-interacting level for small twist angle. Here we only consider interlayer hopping for two neighboring layers. The continuum model describing the $\mu = \mp$ valley is:

$$H_{ATMG}^\mu = \begin{pmatrix} H_N^\mu & \mathbb{U}_\mu^\dagger e^{-i\mu\Delta\mathbf{K}\cdot\mathbf{r}} & 0 \\ \mathbb{U}_\mu e^{i\mu\Delta\mathbf{K}\cdot\mathbf{r}} & H_L^\mu & \mathbb{U}_\mu e^{i\mu\Delta\mathbf{K}\cdot\mathbf{r}} \\ 0 & \mathbb{U}_\mu^\dagger e^{-i\mu\Delta\mathbf{K}\cdot\mathbf{r}} & H_M^\mu \end{pmatrix} \quad (20)$$

where H_N^μ , H_L^μ and H_M^μ are the Hamiltonians of the untwisted bilayers. We only consider the nearest-neighbor interlayer coupling between the two untwisted layers.

$$H_M^\mu = \begin{pmatrix} h_0^\mu(\mathbf{k}) & h_\alpha & 0 & 0 & \cdots \\ h_\alpha^\dagger & h_0^\mu(\mathbf{k}) & h_\alpha & 0 & \cdots \\ 0 & h_\alpha^\dagger & h_0^\mu(\mathbf{k}) & h_\alpha & \cdots \\ & & & \ddots & \end{pmatrix} \quad (21)$$

where $h_0^\mu(\mathbf{k}) = -\hbar v_F(\mathbf{k} - \mathbf{K}_M) \cdot \boldsymbol{\sigma}^\mu$, $\boldsymbol{\sigma}^\mu = (\mu\sigma_x, \mu\sigma_y)$. h_α is the interlayer hopping matrix for different stacking chirality, where $\alpha, \alpha' = +, -$, $h_- = h_+^\dagger$. If we only consider nearest neighbor hopping, the hopping matrix is:

$$h_+ = \begin{pmatrix} 0 & 0 \\ t_\perp & 0 \end{pmatrix} \quad (22)$$

Taking further neighbor hopping for untwisted layers into account, the flat bands will be more dispersive. The hopping matrix is:

$$h_+ = \begin{pmatrix} t_2 f(\mathbf{k}) & t_2 f^*(\mathbf{k}) \\ t_\perp - 3t_3 & t_2 f(\mathbf{k}) \end{pmatrix} \quad (23)$$

we set $t_\perp = 0.48 \text{ eV}$, $t_2 = 0.21 \text{ eV}$, $t_3 = 0.05 \text{ eV}$. The phase factor is $f(\mathbf{k}) = e^{-i\sqrt{3}k_y a/3} + e^{i(k_x a/2 + \sqrt{6}k_y a/6)} + e^{i(-k_x a/2 + \sqrt{3}k_y a/6)}$ ⁵⁸.

\mathbb{U} is the interlayer hopping between two sequences, here we only consider hopping between two neighboring layers.

$$\mathbb{U}e^{-i\Delta\mathbf{K}\cdot\mathbf{r}} = \begin{pmatrix} 0 & \cdots & 0 \\ \vdots & \cdots & \vdots \\ U(\mathbf{r})e^{-i\Delta\mathbf{K}\cdot\mathbf{r}} & \cdots & 0 \end{pmatrix} \quad (24)$$

where $U(\mathbf{r})$ describes the hopping induced by moiré pattern.:

$$U(\mathbf{r}) = \begin{pmatrix} u_0g(\mathbf{r}) & u'_0g(\mathbf{r} - \mathbf{r}_{AB}) \\ u'_0g(\mathbf{r} + \mathbf{r}_{AB}) & u_0g(\mathbf{r}) \end{pmatrix} \quad (25)$$

where $\mathbf{r}_{AB} = (\sqrt{3}L_s/3, 0)$. Because of the corrugation effect, the intrasublattice interlayer hopping term u_0 is different from the intersublattice interlayer hopping term u'_0 ⁷⁸. $g(\mathbf{r}) = \sum_{j=1}^3 e^{i\mathbf{q}_j\cdot\mathbf{r}}$, and $\mathbf{q}_1 = (0, 2/3) \cdot 2\pi/L_s$, $\mathbf{q}_2 = (-1/\sqrt{3}, -1/3) \cdot 2\pi/L_s$ and $\mathbf{q}_3 = (1/\sqrt{3}, -1/3) \cdot 2\pi/L_s$. $\Delta\mathbf{K} = \mathbf{K}_2 - \mathbf{K}_1 = (0, 2/3) \cdot 2\pi/L_s$ is the shift between Dirac fermion from two twisted layers.

II The simplified $\mathbf{k} \cdot \mathbf{p}$ model

Here we provide the expression of \tilde{h}_+ in Eq. 10. Since we only consider the nearest neighbor hopping term in the chiral limit, the interlayer hopping matrix would couple the A(B) sublattice of one layer and B(A) sublattice. For coupling between Dirac fermion of top monolayer graphene and the zero modes from alternating twisted layers, the Dirac fermion from A(B) sublattice is coupled to two wave functions from B(A) sublattice. To be specific, we first consider the coupling between the Bloch state spinor in topmost layer, denoted as $(u_{t,A}(\mathbf{r})e^{i\mathbf{K}_1\cdot\mathbf{r}}, u_{t,B}(\mathbf{r})e^{i\mathbf{K}_1\cdot\mathbf{r}})^T$, and the zero-mode wave function $(\Psi_{\alpha s, \mathbf{k}}(\mathbf{r}), \Psi_{\gamma s, \mathbf{k}}(\mathbf{r}))^T$, where $s = A, B$ is the sublattice indices, and the superscript “ T ” for transpose conjugation. The renormalized hopping matrix between $u_{t,s}(\mathbf{r})e^{i\mathbf{K}_1\cdot\mathbf{r}}$ and $\Psi_{ls, \mathbf{k}}(\mathbf{r})$, is expressed as:

$$\begin{aligned} \tilde{h}_{+, ss'}^t &= (u_{t,s}(\mathbf{r})e^{i\mathbf{K}_1\cdot\mathbf{r}}, 0, 0, 0, 0) \begin{pmatrix} 0 & 0 & h_+ & h_+ & 0 \\ 0 & 0 & 0 & 0 & 0 \\ h_- & 0 & 0 & 0 & h_{+(-)} \\ h_- & 0 & 0 & 0 & h_{+(-)} \\ 0 & 0 & h_{-(+)} & h_{-(+)} & 0 \end{pmatrix} \begin{pmatrix} 0 \\ \Psi_{\alpha s', \mathbf{k}}(\mathbf{r}) \\ 0 \\ \Psi_{\gamma s', \mathbf{k}}(\mathbf{r}) \\ 0 \end{pmatrix} \\ &= \int d\mathbf{r} u_{t,s}^*(\mathbf{r})e^{-i\mathbf{K}_1\cdot\mathbf{r}} h_+ \Psi_{\gamma s', \mathbf{k}}(\mathbf{r}) \\ &= \int d\mathbf{r} u_{t,s}^*(\mathbf{r})e^{-i\mathbf{K}_1\cdot\mathbf{r}} h_+ \left(\frac{1}{\sqrt{2}} \Psi_{Ns', \mathbf{k}}(\mathbf{r}) + \frac{1}{\sqrt{2}} \Psi_{Ms', \mathbf{k}}(\mathbf{r}) \right) \\ &= \frac{1}{\sqrt{2}} \int d\mathbf{r} u_{t,s}^*(\mathbf{r})e^{-i\mathbf{K}_1\cdot\mathbf{r}} t_{\perp} \Psi_{Ns', \mathbf{k}}(\mathbf{r}) \delta_{s,B} \delta_{s',A} \\ &= \frac{1}{\sqrt{2}} \tilde{t}_{\perp} \delta_{s,B} \delta_{s',A} \end{aligned} \quad (26)$$

where t_{\perp} is the interlayer intersublattice hopping parameter between two Dirac fermions. We decompose the zero modes wave function into layer basis. Since we only consider the interlayer hopping between adjacent layers, there is zero overlap between states in topmost layer and zero modes solution in M sequence. The coupling between the zero modes wave function and states from the bottom-most layer can be evaluated in a similar way:

$$\begin{aligned} \tilde{h}_{+, ss'}^b &= (0, \Psi_{\alpha s, \mathbf{k}}(\mathbf{r}), 0, \Psi_{\gamma s, \mathbf{k}}(\mathbf{r}), 0) \begin{pmatrix} 0 & 0 & h_+ & h_+ & 0 \\ 0 & 0 & 0 & 0 & 0 \\ h_- & 0 & 0 & 0 & h_+ \\ h_- & 0 & 0 & 0 & h_+ \\ 0 & 0 & h_- & h_- & 0 \end{pmatrix} \begin{pmatrix} 0 \\ 0 \\ 0 \\ 0 \\ u_{b,s'}(\mathbf{r})e^{i\mathbf{K}_1\cdot\mathbf{r}} \end{pmatrix} \\ &= \frac{1}{\sqrt{2}} \int d\mathbf{r} \Psi_{Ns, \mathbf{k}}^*(\mathbf{r}) \delta_{s,B} \delta_{s',A} t_{\perp} u_{b,s'}(\mathbf{r})e^{i\mathbf{K}_1\cdot\mathbf{r}} \\ &= \frac{1}{\sqrt{2}} \tilde{t}_{\perp} \delta_{s,B} \delta_{s',A} \end{aligned} \quad (27)$$

The explicit expressions of zero modes spinor from two sublattice are²³:

$$\begin{aligned}\Psi_{lA,\mathbf{k}}(\mathbf{r}) &= \frac{\vartheta_{(\mathbf{ka}_1/2\pi)-\frac{1}{6},\frac{1}{6}}-(\mathbf{ka}_2/2\pi)((x+iy)/(a_{2,x}+ia_{2,y})|e^{i2\pi/3})}{\vartheta_{-\frac{1}{6},\frac{1}{6}}((x+iy)/(a_{1,x}+ia_{1,y})|e^{i2\pi/3})} \begin{pmatrix} \bar{\psi}_{\alpha A\mathbf{K}}(\mathbf{r}) \\ \bar{\psi}_{\gamma A\mathbf{K}}(\mathbf{r}) \end{pmatrix}, \\ \Psi_{lB,\mathbf{k}}(\mathbf{r}) &= \frac{\vartheta_{(\mathbf{ka}_1/2\pi)-\frac{1}{6},\frac{1}{6}}-(\mathbf{ka}_2/2\pi)((-x-iy)/(a_{2,x}+ia_{2,y})|e^{i2\pi/3})}{\vartheta_{-\frac{1}{6},\frac{1}{6}}((-x-iy)/(a_{1,x}+ia_{1,y})|e^{i2\pi/3})} \begin{pmatrix} \bar{\psi}_{\alpha B\mathbf{K}}(\mathbf{r}) \\ \bar{\psi}_{\gamma B\mathbf{K}}(\mathbf{r}) \end{pmatrix},\end{aligned}\quad (28)$$

where $l = \alpha, \gamma$, $\vartheta_{a,b}(x+iy|\tau) = \sum_{n=-\infty}^{\infty} e^{i\pi\tau(n+a)^2} e^{2\pi i(n+a)(n+b)}$, $\mathbf{a}_1, \mathbf{a}_2$ are the moiré supercell lattice vector.

III The Coulomb interaction in the twisted graphene

We consider the density-density Coulomb interaction in real space in graphene system:

$$H_C = \frac{1}{2} \sum_{ij} \sum_{\alpha\beta} \sum_{\sigma\sigma'} \hat{c}_{i\alpha\sigma}^\dagger \hat{c}_{j\beta\sigma'}^\dagger U_{ij}^{\alpha\beta} \hat{c}_{j\beta\sigma'} \hat{c}_{i\alpha\sigma}, \quad (29)$$

where i, j are the atomic lattice vector indices, α, β are the sublattice and layer indices, σ is spin index. $U_{ij}^{\alpha\beta}$ is the density-density interaction between two electrons, one at site i layer/sublattice α and the other at site j layer/sublattice β . We can separate the Coulomb interaction into inter-site and on-site term. Since the charge density is quite low in moiré super cell for electrons from flat bands, we can neglect on-site Hubbard interaction, which is at least an order of magnitude smaller than the inter-site ones after projecting on the low-energy states on the moiré length scale⁷⁹. We take Fourier transformation to the real space electron field operator:

$$\hat{c}_{i\alpha\sigma} = \frac{1}{\sqrt{N_s}} \sum_{\mathbf{k}_a} e^{i\mathbf{k}\cdot\mathbf{R}_i} \hat{c}_{\mathbf{k}_a\alpha\sigma} \quad (30)$$

\mathbf{k}_a is the wave vector in atomic Brillouin zone, N_s is the number of atomic unit cells. We can expand the low energy states for twisted graphene around the atomic wave vector, i.e $\mathbf{k}_a = \mathbf{k} + \mathbf{K}$, where \mathbf{k} is the wave vector in moiré Brillouin zone, \mathbf{K} is the moiré reciprocal lattice vector. Then the inter-site Coulomb interaction can be divided into inter-valley term and intravalley term⁵⁹:

$$\begin{aligned}H_C^{\text{intra}} &= \frac{1}{2N_s} \sum_{\alpha\alpha'} \sum_{\mu\mu',\sigma\sigma'} \sum_{\mathbf{k}_a\mathbf{k}'_a\mathbf{q}_a} V(\mathbf{q}_a) \hat{c}_{\mathbf{k}_a+\mathbf{q}_a,\mu\sigma\alpha}^\dagger \hat{c}_{\mathbf{k}'_a-\mathbf{q}_a,\mu'\sigma'\alpha'}^\dagger \hat{c}_{\mathbf{k}'_a,\mu'\sigma'\alpha'} \hat{c}_{\mathbf{k}_a,\mu\sigma\alpha}, \\ H_C^{\text{inter}} &= \frac{1}{2N_s} \sum_{\alpha\alpha'} \sum_{\mu,\sigma\sigma'} \sum_{\mathbf{k}_a\mathbf{k}'_a\mathbf{q}_a} V(|\mathbf{K}-\mathbf{K}'|) \hat{c}_{\mathbf{k}_a+\mathbf{q}_a,\mu\sigma\alpha}^\dagger \hat{c}_{\mathbf{k}'_a-\mathbf{q}_a,-\mu\sigma'\alpha'}^\dagger \hat{c}_{\mathbf{k}'_a,\mu\sigma'\alpha'} \hat{c}_{\mathbf{k}_a,-\mu\sigma\alpha}.\end{aligned}\quad (31)$$

To reach a realistic situation, we consider the screening effect from the device: the single-gate screened Coulomb interaction is $V(\mathbf{q}_a) = e^2(1 - e^{-2|\mathbf{q}_a|d_s})/(2\Omega_M\epsilon_{\text{BN}}|\mathbf{q}_a|)$, where Ω_M is the area of moiré unit cell, $d_s = 400 \text{ \AA}$ is the distance between graphene and gate and ϵ_{BN} is the dielectric constant of h-BN. We can evaluate the energy scale intervalley and intravalley Coulomb interaction: the typical intravalley interaction energy $V_M \approx 25 \text{ meV}$ for $\theta \approx 1.2^\circ$, while the intervalley interaction energy $V(|\mathbf{K}-\mathbf{K}'|) \sim 0.35 \text{ meV}$ for $\theta \approx 1.2^\circ$. As a result, we only consider intravalley Coulomb interaction in our calculation.

We can project the interaction from the original basis to the band basis through the following transformation:

$$\hat{c}_{\mathbf{k}_a,\mu\alpha\sigma} = \sum_n C_{\mu\alpha\mathbf{G},n}(\mathbf{k}) \hat{c}_{\mu\sigma,n\mathbf{k}} \quad (32)$$

where $C_{\mu\alpha\mathbf{G},n}(\mathbf{k})$ is the expansion coefficient in the n -th Bloch eigenstate at moiré wave vector near valley μ , and the summation over the band index n is restricted to the flat-band subspace. We can rewrite the intravalley interaction by applying above transformation:

$$H^{\text{intra}} = \frac{1}{2N_s} \sum_{\mathbf{k}\mathbf{k}'\mathbf{q}} \sum_{\mu\mu'} \sum_{\substack{nm \\ \sigma\sigma'}} \left(\sum_{\mathbf{Q}} V(\mathbf{Q}+\mathbf{q}) \Omega_{nm,n'm'}^{\mu\sigma,\mu'\sigma'}(\mathbf{k},\mathbf{k}',\mathbf{q},\mathbf{Q}) \right) \hat{c}_{\mu\sigma,n\mathbf{k}+\mathbf{q}}^\dagger \hat{c}_{\mu'\sigma',n'\mathbf{k}'-\mathbf{q}}^\dagger \hat{c}_{\mu'\sigma',m'\mathbf{k}'} \hat{c}_{\mu\sigma,m\mathbf{k}} \quad (33)$$

where $\Omega_{nm,n'm'}^{\mu\sigma,\mu'\sigma'}$ is:

$$\Omega_{nm,n'm'}^{\mu\sigma,\mu'\sigma'}(\mathbf{k}, \mathbf{k}', \mathbf{q}, \mathbf{Q}) = \sum_{\alpha\alpha'\mathbf{G}\mathbf{G}'} C_{\mu\sigma\alpha\mathbf{G}+\mathbf{Q},n}^* (\mathbf{k} + \mathbf{q}) C_{\mu'\sigma'\alpha'\mathbf{G}'-\mathbf{Q},n'}^* (\mathbf{k}' - \mathbf{q}) C_{\mu'\sigma'\alpha'\mathbf{G}',m'} (\mathbf{k}') C_{\mu\sigma\alpha\mathbf{G},m} (\mathbf{k}) \quad (34)$$

We can make Hartree-Fock approximation to the intersite intravalley Coulomb interaction so that the two-particle interaction can be solved in a mean-field single particle Hamiltonian. The Hartree term is:

$$H_H^{\text{intra}} = \frac{1}{2N_s} \sum_{\mathbf{k}\mathbf{k}'} \sum_{\substack{\mu\mu' \\ \sigma\sigma'}} \sum_{\substack{nm \\ n'm'}} \left(\sum_{\mathbf{Q}} V(\mathbf{Q}) \Omega_{nm,n'm'}^{\mu\sigma,\mu'\sigma'}(\mathbf{k}, \mathbf{k}', 0, \mathbf{Q}) \right) \quad (35)$$

$$\times \left(\langle \hat{c}_{\mu\sigma,n\mathbf{k}}^\dagger \hat{c}_{\mu\sigma,m\mathbf{k}} \rangle \hat{c}_{\mu'\sigma',n'\mathbf{k}'}^\dagger \hat{c}_{\mu'\sigma',m'\mathbf{k}'} + \langle \hat{c}_{\mu'\sigma',n'\mathbf{k}'}^\dagger \hat{c}_{\mu'\sigma',m'\mathbf{k}'} \rangle \hat{c}_{\mu\sigma,n\mathbf{k}}^\dagger \hat{c}_{\mu\sigma,m\mathbf{k}} \right)$$

and the Fock term is:

$$H_F^{\text{intra}} = - \frac{1}{2N_s} \sum_{\mathbf{k}\mathbf{k}'} \sum_{\substack{\mu\mu' \\ \sigma\sigma'}} \sum_{\substack{nm \\ n'm'}} \left(\sum_{\mathbf{Q}} V(\mathbf{k}' - \mathbf{k} + \mathbf{Q}) \Omega_{nm,n'm'}^{\mu\sigma,\mu'\sigma'}(\mathbf{k}, \mathbf{k}', \mathbf{k}' - \mathbf{k}, \mathbf{Q}) \right) \quad (36)$$

$$\times \left(\langle \hat{c}_{\mu\sigma,n\mathbf{k}}^\dagger \hat{c}_{\mu'\sigma',m'\mathbf{k}'} \rangle \hat{c}_{\mu'\sigma',n'\mathbf{k}'}^\dagger \hat{c}_{\mu\sigma,m\mathbf{k}} + \langle \hat{c}_{\mu'\sigma',n'\mathbf{k}'}^\dagger \hat{c}_{\mu\sigma,m\mathbf{k}} \rangle \hat{c}_{\mu\sigma,n\mathbf{k}}^\dagger \hat{c}_{\mu'\sigma',m'\mathbf{k}'} \right).$$

IV Constraint random phase approximation

The Coulomb interaction in previous section is screened by device, as a result, the Coulomb interaction in reciprocal space is not a Thomas-Fermi form but a single-gate screened from. In this section, we consider further screening effects in band basis. To be specific, the interaction between electrons in flat bands can be screened by virtual excitation of particle-hole pairs from the remote bands. Such screening effects are evaluated by constrained random phase approximation(cRPA). We consider the bubble diagram for screened Coulomb interaction:

$$V_{\mathbf{k}\mu nm, \mathbf{k}'\mu' m' n'}^{cRPA}(\mathbf{q}) = V_{\mathbf{k}\mu nm, \mathbf{k}'\mu' m' n'}^0(\mathbf{q}) \quad (37)$$

$$+ \frac{-2}{N_k} \sum_{n_1 m_1} \sum_{\mathbf{k}_1 \mu_1} V_{k\mu nm, \mathbf{k}_1 \mu_1 m_1 n_1}^0 \chi_{\mathbf{k}_1 \mu_1 m_1 n_1}^0(\mathbf{q}) V_{\mathbf{k}_1 \mu_1 m_1 n_1, \mathbf{k}'\mu' m' n'}^0$$

$$+ \left(\frac{-2}{N_s} \right)^2 \sum_{\substack{n_1 m_1 \\ n_2 m_2}} \sum_{\mu_1 \mu_2} \sum_{\mathbf{k}_1 \mathbf{k}_2} V_{k\mu nm, \mathbf{k}_1 \mu_1 m_1 n_1}^0 \chi_{\mathbf{k}_1 \mu_1 m_1 n_1}^0(\mathbf{q}) V_{\mathbf{k}_1 \mu_1 m_1 n_1, \mathbf{k}_2 \mu_2 m_2 n_2}^0 \chi_{\mathbf{k}_2 \mu_2 m_2 n_2}^0(\mathbf{q}) V_{\mathbf{k}_2 \mu_2 m_2 n_2, \mathbf{k}'\mu' m' n'}^0$$

$$+ \dots$$

We can define the single-gate screened Coulomb interaction projected to flat bands subspace:

$$V_{\mathbf{k}\mu nm, \mathbf{k}'\mu' m' n'}^0(\mathbf{q}) = \sum_{\mathbf{Q}} V(\mathbf{q} + \mathbf{Q}) \lambda_{\mathbf{k}\mu nm}(\mathbf{q}, \mathbf{Q}) \lambda_{\mathbf{k}'\mu' m' n'}^* \quad (38)$$

$$\lambda_{\mathbf{k}\mu nm}(\mathbf{q}, \mathbf{Q}) = \sum_{\alpha\mathbf{G}} C_{\mu\alpha\mathbf{G}+\mathbf{Q},n}^* (\mathbf{k} + \mathbf{q}) C_{\mu\alpha\mathbf{G},m} (\mathbf{k} + \mathbf{q}) \quad (39)$$

where \mathbf{G} is the moire reciprocal lattice vector. The summation of band indices in Eq. (38) is restricted: m_1 and n_1 can not both come from the flat bands subspace. The remote bands below the flat bands are filled, while remote bands above the flat bands are empty. That is to say, the virtual excitation can happen through three channel: from the remote bands below the CNP to flat bands; from flat bands to the remote bands above CNP; from remote bands below CNP to flat bands above CNP. We can define the bare susceptibility in the transferred reciprocal vectors basis $\chi_{\mathbf{Q}, \mathbf{Q}'}^0$ as:

$$\chi_{\mathbf{Q}, \mathbf{Q}'}^0 = \frac{2}{N_k} \sum_{\mathbf{k}} \sum_{\substack{\mu_1 m_1 n_1}} \lambda^\dagger(\mathbf{q}, \mathbf{Q})_{\mathbf{k}_1 \mu_1 m_1 n_1} \chi_{\mathbf{k}_1 \mu_1 m_1 n_1}^0(\mathbf{q}) \lambda(\mathbf{q}, \mathbf{Q}')_{\mathbf{k}_1 \mu_1 m_1 n_1} \quad (40)$$

where:

$$\chi_{\mathbf{k},\mu,m,n}^0(\mathbf{q},\nu) = \frac{f(E_{\mu,m,\mathbf{k}+\mathbf{q}}) - f(E_{\mu,n,\mathbf{k}})}{E_{\mu,n,\mathbf{k}} + \nu - E_{\mu,m,\mathbf{k}+\mathbf{q}}} \quad (41)$$

where μ is valley, \mathbf{k} is wave vector in moiré Brillouin zone, m and n are band indices. Here we only consider static susceptibility, i.e $\nu = 0$. We can rewrite the screened Coulomb interaction in matrix form:

$$\hat{V}^{cRPA}(\mathbf{q}) = \hat{V}(\mathbf{q})_{\mathbf{Q},\mathbf{Q}} \delta_{\mathbf{Q},\mathbf{Q}'} \quad (42)$$

$$\begin{aligned} &+ \hat{V}(\mathbf{q})_{\mathbf{Q},\mathbf{Q}} (-\chi_{\mathbf{Q},\mathbf{Q}'}^0) \hat{V}(\mathbf{q})_{\mathbf{Q}',\mathbf{Q}'} \\ &+ \sum_{\mathbf{Q}''} \hat{V}(\mathbf{q})_{\mathbf{Q},\mathbf{Q}} (-\chi_{\mathbf{Q},\mathbf{Q}''}^0) \hat{V}(\mathbf{q})_{\mathbf{Q}'',\mathbf{Q}'} (-\chi_{\mathbf{Q}'',\mathbf{Q}'}^0) \hat{V}(\mathbf{q})_{\mathbf{Q}',\mathbf{Q}'} \\ &+ \dots \\ &= \hat{V}^0(\mathbf{q}) \cdot (\mathbb{1} + \chi^0(\mathbf{q}) \cdot \hat{V}^0(\mathbf{q}))^{-1} \end{aligned} \quad (43)$$

We define the dielectric matrix as:

$$\hat{\epsilon}^{cRPA}(\mathbf{q})_{\mathbf{Q},\mathbf{Q}'} = (\mathbb{1} + \chi^0(\mathbf{q}) \cdot V^0(\mathbf{q}))_{\mathbf{Q},\mathbf{Q}'} \quad (44)$$

We can make Hartree-Fock approximation to the screened Coulomb interaction and decomposed into two terms. For the Hartree term, we take $\hat{V}^{cRPA}(\mathbf{q} = 0)$, while we take $V(\mathbf{k}' - \mathbf{k} + \mathbf{Q})/\epsilon(\mathbf{k}' - \mathbf{k} + \mathbf{Q})$ for the Fock term.